Contents lists available at ScienceDirect

Thermal Science and Engineering Progress

A chemical reactor network approach for a gas-assisted iron dust flame in a laboratory-scale combustor

Sören Dübal [a,b], Pascal Steffens [b], Johannes Mich [b], Daniel Braig [b], Antje Vahl [b], Leon L. Berkel [b], Arne Scholtissek [b], Tiziano Faravelli [c], Christian Hasse [b], Hendrik Nicolai [b,*], Sandra Hartl [d]

[a] *Department of Mechanical and Plastics Engineering, a, Schöfferstraße 3, Darmstadt, 64295, Germany*
[b] *Simulation of Reactive Thermo-Fluid Systems, Technical University of Darmstadt, Otto-Berndt-Str. 2, Darmstadt, 64287, Germany*
[c] *Department of Chemistry, Materials and Chemical Engineering, c, Piazza Leonardo Da Vinci 32, Milan, 20133, Italy*
[d] *Faculty Mechanical and Systems Engineering, University of Applied Sciences Esslingen, Kanalstraße 33, Esslingen, 73728, Germany*

ARTICLE INFO

ABSTRACT

Metal powders demonstrate promising performance when reacting with oxygen in laboratory-scale reactors, releasing the chemically stored energy as heat. To scale up this technology, chemical reactor network (CRN) modeling serves as a critical tool to bridge the gap between laboratory experiments and real-world applications. In this work, a multi-phase CRN is derived to analyze the iron oxidation and pollutant formation in a novel methane-assisted iron dust flame in a laboratory-scale combustor. State-of-the-art single particle oxidation models are employed to describe the conversion of iron particles, while gas phase combustion is modeled with a detailed kinetic mechanism within fully coupled reactors. The approach is validated for single particle combustion using the solid-gas plug flow reactor. It is demonstrated, that a reactor network model with four solid-gas perfectly stirred reactors accurately reproduces the flame structure of laminar iron flames. Subsequently, both ideal reactor models are combined in a multi-phase reactor network to analyze iron oxidation, evaporation and NOx formation in the swirl burner. The CRN design is based on a recent high-fidelity Large Eddy Simulation. The monodisperse description of the iron suspension within the CRN reveals that different initial particle diameters significantly influence the estimated evaporated mass, ranging from less than 0.5% for 20 μm particles to approximately 4% for 5 μm particles, while the overall iron conversion remains largely unaffected. Furthermore, sensitivity analyses highlight the critical role of the oxygen distribution and local gas temperatures within the reactor to effectively control NOx formation and potential nano-oxide emissions during iron combustion.

1. Introduction

Recent studies demonstrate that metal fuels have enormous potential as carbon-free energy carriers to boost the energy transition in retrofitted power plants [1–4]. One particularly promising metal fuel is iron powder, as it is non-toxic, possesses a high energy density, and is already produced in large quantities [5]. The chemical energy stored within the iron microparticles can be released through heterogeneous combustion, resulting in the formation of solid iron oxides. Subsequently, the oxide particles can be collected and reduced using green hydrogen, enabling the long-term storage of renewable energy. The global process forms a carbon-free circular economy.

To facilitate the rapid implementation of the iron energy cycle in industry, a simulation-guided design and retrofit of power plants is highly desirable. However, in comparison to established carbonaceous solid fuels, iron burns in a heterogeneous mode, which poses a variety of challenges for modeling [6].

Fig. 1 depicts physical and chemical processes during the combustion of micron-sized iron particles. In order to predict the combustion of iron particles, it is necessary to consider chemical kinetics for the heterogeneous reactions occurring across multiple oxidation states, starting from Wüstite (FeO), over Magnetite (Fe_3O_4) up to Hematite (Fe_2O_3). The chemical kinetics must be combined with an accurate description of heat and mass transfer in differing combustion regimes. During conversion, the iron particles can undergo several phase transitions such as melting and, at elevated particle temperatures, evaporation, which entails the formation of nano-oxides as particulate pollutants. Finally, the liquid iron(-oxides) solidify and form a solid oxide particle.
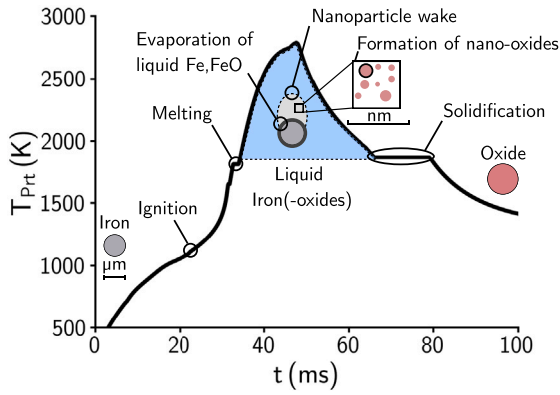

Fig. 1. Schematic of physical and chemical processes during iron particle combustion, based on results of a single particle simulation from [7].

A focus of recent numerical studies is the flame propagation investigating different propagation regimes [8,9], and effects of turbulence [10,11] and polydisperse suspensions [12] on iron dust flames. In the case of a binary fuel mixture (e.g. gas assistance), not only solid conversion but also gas phase combustion needs to be included within the modeling framework.

Hence, significant endeavors are being made to create innovative models tailored for Computational Fluid Dynamics (CFD) applications [7,13–16]. The goal is to facilitate high-fidelity simulation frameworks, a capability already established for carbonaceous fuels [17,18]. Despite the growing effort over the last few years, mostly fundamental numerical [8–12,19–21] and experimental [22–27] studies have been carried out.

One of the few laboratory-scale validation experiments, accompanied by the first 3D Large Eddy Simulation (LES) in the context of iron dust flames has been carried out by Steffens et al. [28] to investigate multi-scale processes present in large scale turbulent flames. While the LES offers comprehensive insights into flame characteristics, the current computational resources limit the scope of broad design studies for the rapid development of technical combustion systems. The intricate physical and chemical processes on the single particle scale, mixing of the multi-phase flow, and pollutant formation present potential barriers for large-scale application of CFD and suggest the necessity for scale-reduced models.

Scale-reduced modeling approaches employ detailed physical submodels and simultaneously reduce computational costs. In a recent application-oriented study, Thijs et al. [29] analyzed low-emission strategies with a plugflow model for a laboratory-scale iron powder burner. To achieve an accurate pollutant prediction, it is essential to consider local mixing and temperatures.

Chemical reactor network (CRN) modeling allows for the integration of detailed solid and gas-phase chemistry (and advanced pollutant submodels) with a simplified flow structure by dividing technical systems into functional macro zones represented by ideal reactor models [30,31]. The design of a reactor network requires flow and temperature profiles obtained from experimental data and/or CFD simulations. For the combustion of pulverized solid fuels, reactor networks have been successfully extended for predominantly homogeneously burning coal [32] and biomass [33] recently. Pyrolysis and heterogeneous combustion were described with detailed kinetics on a volumetric basis and allow for direct coupling with gas phase mechanisms including a detailed description of pollutant formation [34]. In the context of iron combustion, the CRN approach may prove useful for accurately predicting the formation of nano-oxides from the evaporation of liquid iron(oxides) [23,25,35] and nitrogen oxides (NOx) as gaseous pollutants [29] in comparison to CFD simulations at technically relevant scales.

This paper aims to extend the CRN approach previously presented in [32,33] to model iron dust flames. Due to the physical and chemical complexity of iron combustion, a step-wise approach with three different complexity levels is chosen:

1. The general applicability of ideal reactors to model iron combustion is examined. To this end, two models for iron particle oxidation [7,13] are coupled to the single reactor units and verified with data from single particle combustion.
2. A reactor network approach is presented, which accounts for the flame structure of gas-assisted laminar iron flames.
3. The novel extensions of the CRN approach are applied to the gas-assisted laboratory-scale turbulent iron dust flame based on LES data [28].

The remainder of this work is structured as follows: The relevant modeling concepts with a brief verification of implementations to the CRN framework are introduced in Section 2. Section 3 investigates approaches for accurately modeling the structure of laminar iron flames. Subsequently, the results of a multi-phase reactor network deployed on a methane-assisted iron dust flame in a laboratory-scale combustion chamber are highlighted and discussed in Section 4. The main conclusions of this work are presented in Section 5.

2. Modeling

First, the concept of CRN modeling is introduced, followed by a description of the multi-phase reactor units. Afterward, the incorporation of iron microparticle oxidation into CRN modeling is discussed. To verify the novel implementations, the results from single reactor simulations are compared to reference data of single particle simulations from literature [7,13].

2.1. Chemical reactor network modeling

A CRN consists of multiple ideal reactor models. Primarily, two reactor types describe the characteristic flow behavior of the system under consideration. Regions with strong mixing, such as recirculation zones (RZ), are modeled with a perfectly stirred reactor (PSR), which assumes perfect mixing within its volume. The plug flow reactor model (PFR) is used for straight flow patterns. In addition, auxiliary units for mixing and splitting the mass flows are considered to connect different reactors. In this work, reactor networks consisting of recently introduced multi-phase reactor models [32,33] are employed to describe the heterogeneous processes during iron combustion.

The balance equations for the gas and solid phases for the steady-state s-PFR [32] read:

$$\frac{d\dot{m}_{i,j}}{dz} = \dot{\omega}_{i,j} \cdot \text{MW}_{i,j} \cdot \text{A}_j \qquad \text{with } j = \text{gas, solid.} \tag{1}$$

Eq. (3) describes the change in the mass flow rate $\dot{m}$ of the gaseous and solid species i along the spatial coordinate z via the formation rate $\dot{\omega}$, the areas A of the respective phase and the molar mass MW.

Due to the ideal mixing in the steady-state solid–gas Perfectly Stirred Reactor (s-PSR) model, the balance Eq. (2) is formulated over the reactor volume V

$$\frac{dm_{i,j}}{dt} = \dot{m}_{i,\text{in},j} - \dot{m}_{i,\text{out},j} + \dot{\omega}_{i,j} \cdot \text{MW}_{i,j} \cdot \text{V}_j = 0 \tag{2}$$
$$\text{with } j = \text{gas, solid.}$$

Fig. 2 shows a comparison of the respective conversion mechanisms of solid carbonaceous fuels and iron. Within the multi-phase reactors, gases and solids are directly coupled. Solid fuels, such as coal or biomass, occupy a certain volume and are composed of characteristic reference species, which have distinct reaction pathways for pyrolysis, char formation, and subsequent char oxidation (or gasification) [36,
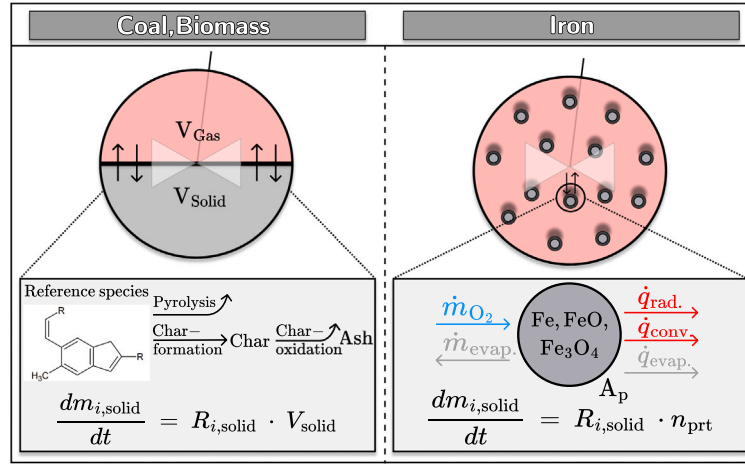
Fig. 2. Representation of solids and the respective conversion mechanisms for solid hydrocarbons (left) and iron (right) within the multi-phase CRNs.

37]. This way, solid conversion can be accurately described with detailed kinetics on a volumetric basis and coupled to detailed gas phase mechanisms [34]. In state-of-the-art numerical studies, the oxidation of iron particles is described by single particle models. In the present work, these models are coupled to the ideal reactor units to account for iron combustion in reactor networks. Thus, the phases in the novel iron reactor models are represented by suspended iron particles in the gas phase, as highlighted in Fig. 2. The iron particle conversion rates are calculated for an average particle size.

During the heterogeneous oxidation, the particles experience a rapid heat-up due to the exothermic reaction with oxygen at the surface. Since the particle heat-up is particularly relevant for the conversion, the change in solid enthalpy flux ($\dot{H}_{\text{solid}}$) is calculated from the change in particle enthalpy (H_{prt}) for the residence time τ within the s-PFR

$$\frac{d\dot{H}_{\text{solid}}}{d\tau} = \frac{dH_{\text{prt}}}{d\tau} \cdot \dot{n}_{\text{prt}}. \tag{3}$$

The balance equation for the steady-state s-PSR reads

$$\frac{d\dot{H}_{\text{solid}}}{dt} = \frac{\dot{H}_{\text{solid,in}} - \dot{H}_{\text{solid,out}}}{\tau} + \frac{dH_{\text{prt}}}{dt} \cdot \dot{n}_{\text{prt}} = 0. \tag{4}$$

The gas temperature is kept constant within the ideal reactors. At elevated temperatures, iron(-oxide) species undergo phase transitions, such as melting and evaporation [23,25], leading to the formation of gaseous iron(-oxide) species. The formation rates of solid and gaseous species, as well as the change in enthalpy from the single particle model are scaled up to the total number flux of iron particles ($\dot{n}_{\text{prt}}$) representing the solid mass flow inside the reactor network as a whole. Within the reactor network, the solid phase is handled as a stream containing mass fractions of iron and the respective oxides (FeO, Fe$_3$O$_4$).

2.2. Solid and gas phase kinetics

In the following, two models for the oxidation of micron-sized iron particles and the gas-phase kinetic mechanism to describe the hybrid iron–methane combustion within the reactor networks are presented.

2.2.1. First-order surface kinetics (FOSK) model

The first particle model is the First Order Surface Kinetics (FOSK) model by Mich et al. [13], which is based on the works by Soo et al. [38, 39] and later model extensions [14,40]. It combines a surface reaction with a boundary layer model for heat and mass transfer and can account for both, kinetically and diffusion-limited combustion. The governing equations are given by [13]:

$$\frac{dm_p}{dt} = \dot{m}_{\text{O2,kin}} = \dot{m}_{\text{O2,diff}} \tag{5}$$

$$\dot{m}_{\text{O2,kin}} = \rho_f \cdot Y_{\text{O2,s}} \cdot A_p \cdot k_\infty \cdot \exp\left(-\frac{T_a}{T_p}\right) \tag{6}$$

$$\dot{m}_{\text{O2,diff}} = \rho_f \cdot A_p \cdot \frac{\text{Sh} \cdot D_{\text{O2,f}}}{d_p} \tag{7}$$

$$\frac{dm_{\text{Fe}}}{dt} = -\frac{1}{s} \frac{dm_p}{dt}. \tag{8}$$

The change in particle mass dm_{p}/dt is related to the oxygen rates based on surface kinetics $\dot{m}_{\text{O2,kin}}$ and diffusion through the boundary layer $\dot{m}_{\text{O2,diff}}$. It is assumed that oxygen diffuses to the particle at the same rate as it is consumed by the chemical reaction. Therefore, both rates need to be equal. An Arrhenius-type equation containing the film density ρ_f, the surface area A_p, a pre-exponential factor k_∞, the activation temperature T_a and the particle temperature T_p describes the reaction with the oxygen concentration $Y_{\text{O2,s}}$ at the particle surface. The Sherwood number Sh, described with the Ranz–Marshall correlation [41], the diffusion coefficient of oxygen in the boundary layer $D_{\text{O2,f}}$ and the particle diameter d_p are used to calculate the diffusive rate with Eq. (7). The stoichiometric ratio s = 0.28 (kg oxygen per kg iron) in Eq. (8) determines the change of the respective iron(-oxide) masses. Within the FOSK model, only the first oxidation step from Fe to FeO is considered. A detailed description of the model is reported in [13].

2.2.2. Reactive cooling (RC) model

The second particle model considered for the reactor networks is based on the Solid Oxide Layer Diffusion (SOLD) model proposed by Mi et al. [15] and has been extended in recent works by Mich et al. [7, 13] to account for reactive cooling of the molten particle and a sub-model for evaporation. A different mechanism compared to the FOSK model is proposed to account for the ignition of iron particles within this approach. The solid phase comprises Fe, FeO, and Fe$_3$O$_4$ in a layered structure from the core to the surface, and the rate-limiting step for oxidation is assumed to be the diffusion of Fe ions through the oxide layers. For the kinetically-limited regime, the equations for the reaction rates of Fe and Fe$_3$O$_4$ are given as follows [7]:

$$\frac{dm_{\text{FeO}}}{dt} = 4\pi \cdot \rho_{\text{FeO}} \cdot \frac{r_{\text{Fe}} r_{\text{FeO}}}{r_{\text{FeO}} - r_{\text{Fe}}} \cdot k_{\infty,\text{FeO}} \cdot \exp\left(-\frac{T_{a,\text{FeO}}}{T_p}\right), \tag{9}$$

$$\frac{dm_{\text{Fe}_3\text{O}_4}}{dt} = 4\pi \cdot \rho_{\text{Fe}_3\text{O}_4} \cdot \frac{r_{\text{FeO}} r_{\text{Fe}_3\text{O}_4}}{r_{\text{Fe}_3\text{O}_4} - r_{\text{FeO}}} \cdot k_{\infty,\text{Fe}_3\text{O}_4} \cdot \exp\left(-\frac{T_{a,\text{Fe}_3\text{O}_4}}{T_p}\right), \tag{10}$$

with the radii r_i and densities ρ_i for the respective layers and $k_{\infty,i}$ and $T_{a,i}$ as kinetic parameters. The aforementioned Sherwood correlation from Eq. (7) is used to model the diffusion-limited regime. After reaching the peak temperature during oxidation, the iron particle has reached an oxidation state between FeO and Fe$_3$O$_4$, leading to further oxidation during the cooling phase. The energy released during the exothermic oxidation process leads to a slower cooling than inert

cooling. Moreover, the model accounts for the evaporation of Fe and FeO, based on the work of Fujinawa et al. [42]. The evaporation rate $\dot{m}_{i,evap}$ is modeled with a Sherwood correlation

$$\dot{m}_{i,\text{evap}} = \rho_f \cdot A_p \cdot \frac{\text{Sh} \cdot D_{O2,f}}{d_p} \cdot (Y_{i,g} - Y_{i,s}), \tag{11}$$

including film and condensed phase properties and the mass fractions of evaporating species. The mass fractions at the particle's surface are given by respective vapor pressures. Within the reactive cooling model, the enthalpy balance is extended by the specific enthalpies of the respective evaporated species. The liquid Fe–O system is represented by mass fractions of the solid stream inside the reactor network (Fe(l) and Fe_xO_y(l)). Further information on the reactive cooling model can be found in [7].

2.2.3. Gas phase kinetics

The formation rates for the gaseous species are calculated from the CRECK-G mechanism [43] on a volumetric basis. Evaporation products are considered within the gas phase mechanism, adapted from kinetic studies on nanoparticle synthesis [44,45]. As a first step, only evaporation into the gas phase is considered. The accurate description of gaseous iron(-oxide) kinetics in iron–air flames and the subsequent formation of nanoparticles remains a topic of ongoing research [35].

2.3. Numerical framework

All of the aforementioned equations are implemented into the academic code NetSMOKE [31,46]. The particle models are coupled to the classes of the ideal reactors and contribute to the formation rates within the species and mass balance equations. In case of recycling streams, the respective reactor equations are solved with a global solution method. To manage complexity, the network is partitioned into strongly connected components (SCCs), allowing each SCC to be solved individually. The resulting system of non-linear equations for an individual SCC is solved with a global solution method. A sequential modular (SM) approach followed by an equation-oriented (EO) approach as reported in [31,32] is employed to ensure convergence. In the SM approach, units are solved sequentially following precedent topological sorting [33]. In EO mode, all equations in an SCC are combined into a single system and solved using the OpenSMOKE++ [2] non-linear equation system (NLS) solver. A detailed description of the global solution method, convergence and stop criterion of the solvers can be found in Refs. [47–49].

2.4. Verification of single particle combustion

To demonstrate the applicability of single reactors to model iron particle combustion, the implementations within NetSMOKE are verified by a comparison with results of single particle simulations reported by Mich et al. [7,13]. The single particle simulations were validated in these previous works in a comparison against experimental data for the combustion of individual particles [22,23,26] in air. A s-PFR is used for this verification case. Fig. 3 shows the temperature (upper row) and the mass fraction profiles (lower row) during single particle oxidation.

In the FOSK simulation (left), the surrounding gas temperature is kept constant at 300 K, and the initial temperature for the 54 μm particle is set to 1500 K. At this elevated particle temperature, the heterogeneous reaction starts immediately resulting in a rapid temperature increase. At approximately 1800 K, iron reaches its melting temperature, and the temperature remains constant throughout the phase transition. Following the melting process, the particle temperature subsequently increases to its peak, where Fe is fully converted to FeO. This is followed by an inert cooling phase.

A similar particle temperature profile is obtained with the reactive cooling simulation (Fig. 3, right). The initial particle size is 49 μm at 300 K with a constant surrounding gas phase at 1350 K. Following the
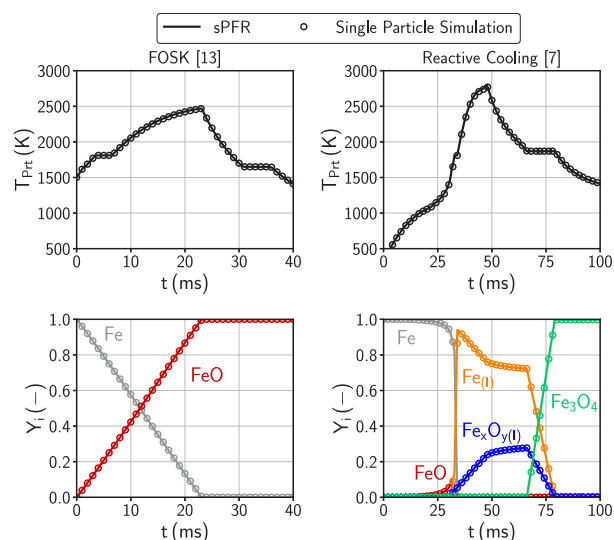

Fig. 3. Verification of the FOSK and Reactive Cooling Model with the s-PFR in NetSMOKE based on temperature (upper) and species profiles (lower).

inert heating phase, the particle temperature increases rapidly, then arrives at a melting plateau, and then increases further until reaching a peak. As illustrated in the species profiles, the formation of liquid iron(-oxide) species occurs during the melting stages. A considerable amount of liquid evaporates at elevated temperatures. The oxidation process persists as the particle cools down. Subsequently, the droplet solidifies as magnetite (Fe_3O_4). The calculated profiles indicate that the novel reactor simulations match the ignition and complex conversion characteristics of the single particle very accurately.

3. CRN modeling of laminar iron flames

Following the successful application of a single reactor to single particle combustion, the complexity is gradually increased through modeling premixed laminar iron flames. As the iron dust flame within the laboratory-scale combustor is methane-assisted, a CRN approach for the accurate representation of combined methane and iron combustion is presented.

3.1. Reference CFD simulations

To provide an overview of the considered configurations, Fig. 4 illustrates the reference laminar flames denoted as (a) and (b). A scheme of the laminar channel (Case: 3D) is depicted in Fig. 4(a). The methane/air mixture, together with iron particles is introduced at the upper portion of the tube. Within the CFD, gas phase combustion is calculated employing the GRI-Mech 3.0 [50] mechanism. To ensure an accurate comparison, the GRI-Mech 3.0 mechanism is employed for the CRN simulations in this section as well.

The second case represents a generic one-dimensional iron–air flame (Case: 1D). Fig. 4(b) displays the relevant characteristics in terms of temperature and oxygen profiles of laminar flames containing micron-sized iron particles. In the reaction zone, the temperature of the particle locally overshoots the gas temperature. After the heterogeneous reaction stops, the particle temperature converges towards the gas temperature. As highlighted by the dashed vertical lines, the oxygen profile indicates the boundaries of the reaction zone, exhibiting a diffusive profile until the peak temperature is attained and the iron is fully converted. In both reference simulations, the FOSK model is employed to describe a monodisperse solid phase in generic flame configurations. An overview of the relevant parameters in the reference simulations is given in Table 1.
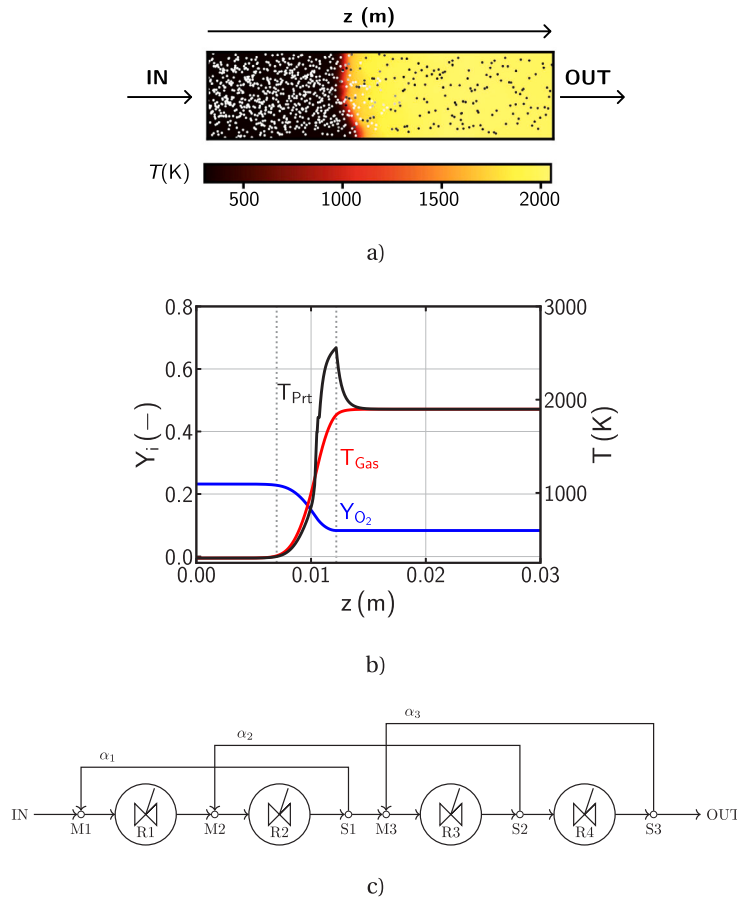
a)

b)

c)

Fig. 4. Reference laminar iron flames. Scheme with gas temperature profile of a laminar methane-assisted iron flame (a) (Case: 3D) and temperature and species profiles of a generic laminar iron–air flame (b) (Case: 1D). The corresponding reactor network representation accounting for the flame structure is displayed in (c).

Table 1
Relevant boundary conditions of the reference CFD simulations. The equivalence ratios are calculated based on the amount of oxygen that can be consumed by iron (and methane) as reported in [13].

Configuration	Surrounding gas	d_{Prt} (μm)	Φ (−)
3D (Pipe)	$N_2/O_2/CH_4$	14.6	0.3
1D [13]	$N_2/O_2/Ar$	30	0.7

3.2. CRN modeling of the flame structure of laminar iron flames

In a first attempt to model laminar iron flames, a single s-PFR simulation, similar to [29], is carried out to match the temperature and species profiles along the z-axis of the pipe simulation in Fig. 4(a). Therefore, the boundary conditions of the laminar flow channel are applied to the s-PFR and its gas temperature profile is set according to the CFD data. Fig. 5 shows a comparison of the temperature (top), iron, and major gaseous species (bottom) profiles between the single reactor and CFD simulation (dotted lines).

The profiles reveal notable differences between the simulations. The combustion of methane is delayed and the gases react immediately at a specific temperature in the s-PFR. In this hybrid iron–methane flame, it is necessary to accurately model the competition for oxygen in order to describe the conversion of the iron particles, as described by other authors [6,28]. The iron particles ignite at an earlier stage and undergo slower conversion than in the reactor simulation. This earlier ignition is also reflected in the particle temperature profile. It is essential to capture the profiles of the gaseous species in the reaction zone, as the film composition is crucial for the enthalpy balance of the particle.

In this case, a single s-PFR simulation, as in the single particle cases, is not a viable approach for modeling the flame structure, as

diffusion is not considered. Therefore, a more intricate reactor network configuration is necessary to accommodate the molecular diffusion of gaseous species. The reactor network should reliably reproduce the mass fraction profiles of gaseous species within the reaction zone of the laminar flame. A schematic representation of the network is provided in Fig. 4(c). The reaction zone is subdivided into discrete sections and modeled by a series of isothermal s-PSRs accompanied by various mixing M_i and (phase-)splitting S_i units to facilitate the simulation of the multiphase flow. Only gases are partially recycled back to the previous reactor, with the amount determined by the splitting ratios α_i. The splitting ratios are optimized in a subroutine, to match the oxygen profiles from the reference simulations. Phase-splitting units [33] separate the iron particles from the backmixed gases. The boundaries of the reaction zone, where the network configuration is applied, are defined based on the mass fraction profiles of gaseous species. The inverse velocity profile from the reference simulations is utilized to determine the residence times of the s-PSR units. Furthermore, the temperatures of the gaseous and solid phases are extracted from the corresponding reference simulations. The influence of the number of reactors is discussed in the following.

Fig. 6 depicts the profiles of solid and major gaseous species obtained from the CRN simulations with varying reactor numbers compared to the reference. As the CRN model only accounts for the reaction zone, the limits of the z-coordinate differ from those shown in Fig. 4(b) for further examination. The markers are positioned at the inlet and outlet of each reactor, respectively. The deviation between the CRN and the reference simulations is indicated by the red areas, explicitly shown for the iron and oxygen mass fraction profiles. In general, a better agreement is obtained with an increase in the number of reactors for both reference simulations. In the iron–methane case, a large portion
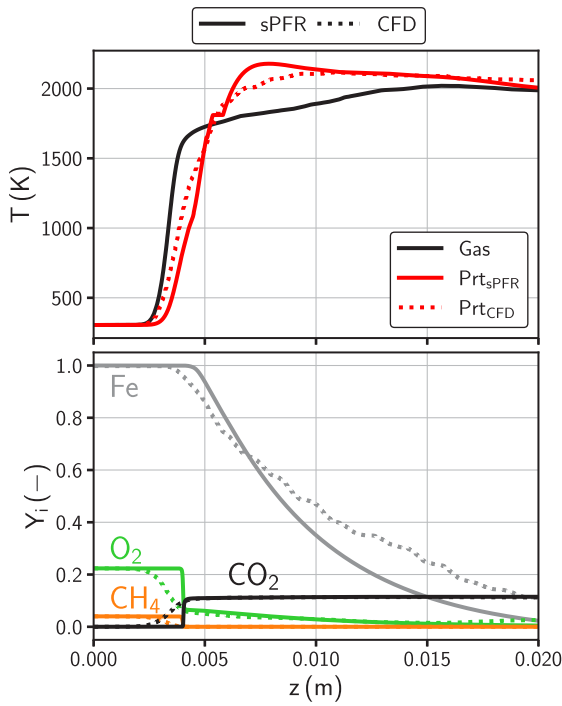
Fig. 5. Particle and gas temperature (top), Iron and major gas species profiles (bottom) from CFD compared to single s-PFR simulations over domain length.

Table 2
Computation times for the laminar flame CRN simulations with varying amounts of reactors (N_R).

Reference	N_R (−)	CPU time (s)
Iron–methane	2	1.95
	4	3.26
	8	4.86
Iron–air [13]	2	0.25
	4	0.90
	8	1.68

of the oxygen is consumed by the methane flame prior to the ignition of the iron particles, which then proceed to consume further oxygen. The computation times of the CRN simulations with two, four, and eight reactors for both reference cases are provided in Table 2. Similar CPU times are obtained with the same amount of sequential solutions, followed by a fully coupled approach. Slightly larger computation times are evident in the methane-assisted case, due to the additional gas phase reactions. Since the agreement increases with the number of reactors, four reactors are suitable to balance the trade-off between the optimal accuracy and the minimum computational effort to recover the laminar flame structure.

4. Gas-assisted turbulent iron dust flame

In this section, a multi-phase reactor network is applied to a laboratory-scale combustion chamber in the context of gas-assisted iron combustion. First, the experimental configuration and reference simulation are presented, followed by the design of the CRN for the iron dust flame. After a reactor network based on the LES data is proposed, iron particle conversion, evaporation as the precursor for particulate pollutants, and NOx formation are analyzed by coupling a detailed particle model for iron oxidation [7] to a detailed gas-phase mechanism [43]. The effects of particle size, flow distribution, and gas temperatures within the network on total iron conversion, evaporation, and NOx formation are investigated through sensitivity studies.
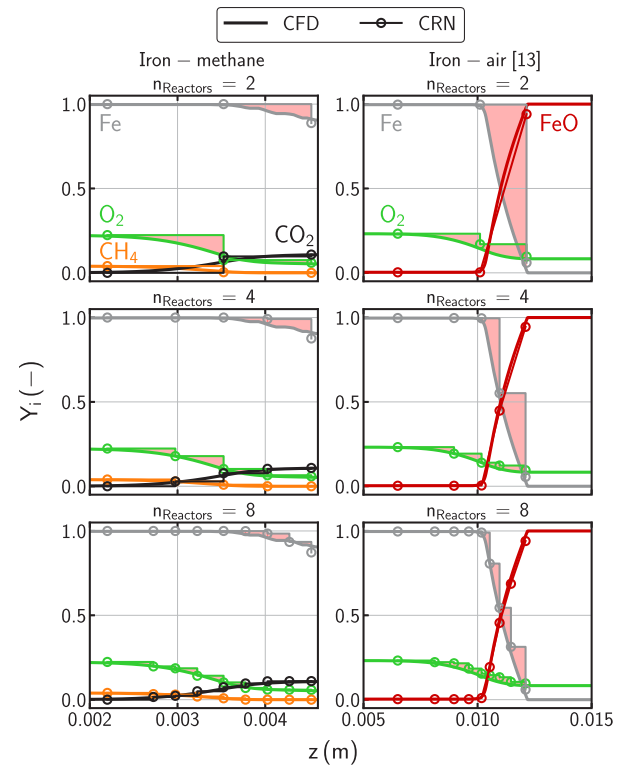

Fig. 6. Species profiles of the CRN simulations with two, four, and eight reactors for the laminar iron–methane (left) and iron–air (right) flames of the reference cases. The deviation between CRN and CFD simulations is implied by the red areas. For visualization purposes, only the deviation of iron and oxygen mass fraction profiles are shown.

Table 3
Iron mass flow and air–fuel ratios (λ) of the iron–methane operating condition [28].

Parameter	Units	
Mass flow iron	(kg h^{-1})	13
Primary flow λ_1	(−)	0.32
Secondary flow λ_{1+2}	(−)	0.61
Total λ_{tot}	(−)	1.25
Oxidizer (O$_2$/N$_2$)	(Mole fraction)	0.21/0.79

4.1. Experiment and reference simulation

A schematic drawing of the laboratory-scale combustion chamber [51] is shown in Fig. 7. Gas-assisted carbonaceous fuel flames have been extensively investigated experimentally [52] and numerically [53,54] in this configuration. The burner has a central, annular inlet through which the primary gas stream and the solid particles are fed into the combustor. A swirled secondary stream transports additional oxidizer into the combustion chamber, where it is mixed with the primary stream in the quarl. The swirl induces a recirculation that recycles hot flue gases, thereby facilitating flame stabilization. A tertiary flow introduced from the side supplies additional oxidizer for overall lean conditions.

Laser diagnostics may be utilized to measure the flow field and species profiles due to optical accessable walls. Particle Image Velocimetry (PIV) measurements have been carried out to investigate the flow field of a methane-assisted iron dust flame [28]. In addition to the experimental data, a LES [28] of the combustion chamber was conducted. The solid particles are described in an Euler–Lagrangian approach, combined with the FOSK model for heterogeneous iron oxidation. The iron kinetics are coupled to a flamelet-based approach for the gas phase. The LES has been validated against the experimental data and serves as the basis for the CRN study. In particular, the flow and
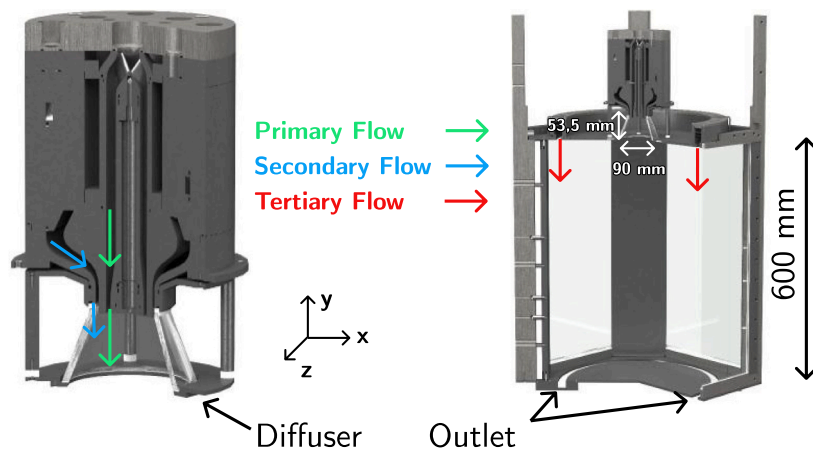
Fig. 7. Experimental configuration of the laboratory-scale combustion chamber, adapted from [51]. Left: Diffusor with primary and secondary flow. Right: Whole chamber with tertiary flow.

temperature fields are used for the design of the reactor network. The considered operating point for experiments and simulations is listed in Table 3.

Within the LES, a particle size distribution of the iron powder is considered. Based on established approaches with one particle size within CRN modeling, the simulations are performed with a mean diameter of d_{50} = 7.7 μm. The conversion behavior of particles of different size is discussed in Section 4.4.

4.2. Reactor network design

The CFD-based CRN design uses information on flow and temperature fields to identify functional macro zones for subdividing the complex combustor volume to apply ideal reactor models for functional compartments [31,32].

Fig. 8 depicts a comparison of the reactor network design on top of the flow (streamlines) and temperature fields for the aforementioned operating point of iron dust combustion. The flow field imposed by the burner design reveals multiple recirculation zones resulting from the burner's geometry and operation. As highlighted in previous works [52,54], a characteristic inner recirculation zone (marked as IRZ) forms inside the diffuser due to the swirled secondary flow. The streamlines further display a large external recirculation zone (ERZ) below the dump plane, extending close to the outlet. Solid–gas perfectly stirred reactors represent the recirculation zones in the multi-phase CRN. Within the reactor network, the large ERZ region is represented by a s-PSR and a s-PFR, which are coupled to the reactors in the center region through a large recycle. The center of the combustor exhibits a straight flow pattern, modeled with solid–gas plug flow reactors. The simplified network structure is displayed on the right side according to the streamlines and temperature field, assuming axial symmetry. Multiple mixing and splitting units (S1 to S6) account for an accurate oxygen distribution inside the combustion chamber, modeling the mixing between the high-temperature flame zone and the colder external recirculation zone with oxygen contents.

In the next step, information from the temperature field of the CFD simulation is used to determine the gas phase temperature in each reactor. Furthermore, averaged temperatures for the solid phase at the reactor inlets are determined from the particle data. In the following, the CRN representation of the diffuser region is described in more detail. An enlarged view of the CRN around the IRZ on top of the temperature and flow fields obtained from CFD is given in the upper right corner in Fig. 8. This section of the CRN models the combined iron–methane flame in this area. Following the findings in Section 3, a single s-PFR unit is not suitable to accurately model the oxygen consumption by the methane flame. Accordingly, the recycle
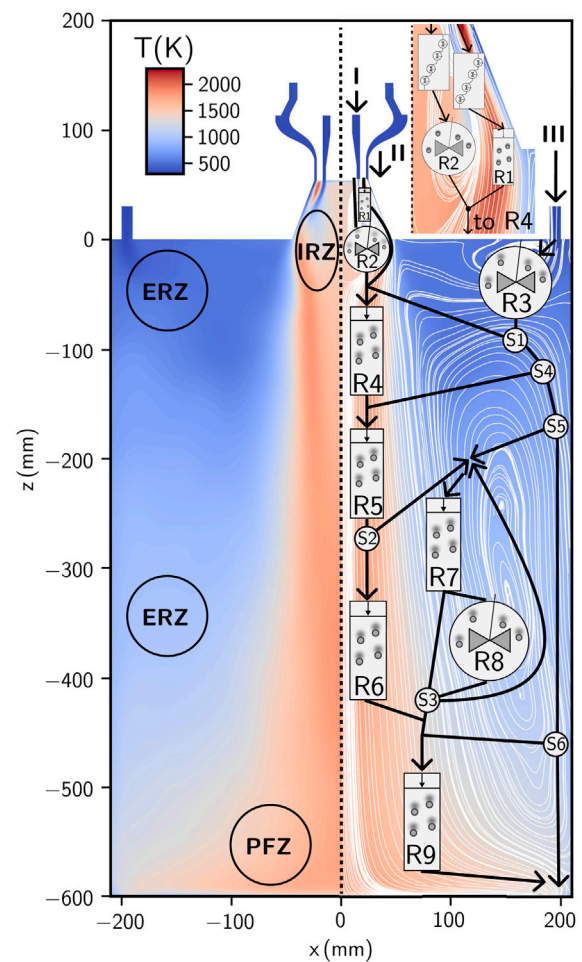

Fig. 8. Temperature and flow fields from reference CFD simulation. A scheme of the corresponding CRN is indicated on top of the CFD fields. Mixing units are not explicitly shown.

network consisting of four s-PSRs is integrated within two discrete units following the inlet. Subsequently, the gases and particles are subjected to elevated temperatures in the bypass area and the IRZ. Further downstream, the reaction zone of the iron dust flame is considered within the iron CRN.
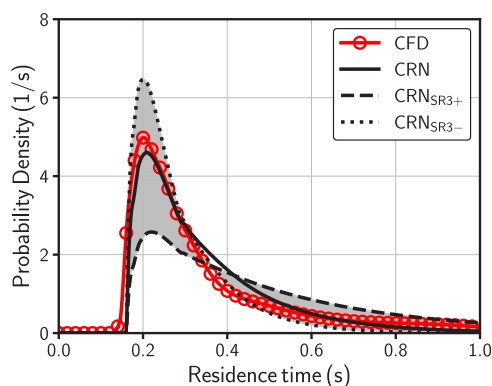
Fig. 9. RTD of the CRN obtained by the optimization procedure (CRN) compared to the probability density function (PDF) of particle ages from CFD. The gray area between the upper (SR3+) and the lower dashed lines (SR3−) indicates the variation in CRN-RTD response for a $\pm 10\%$ change in each splitting ratio for all splitter units of the CRN.
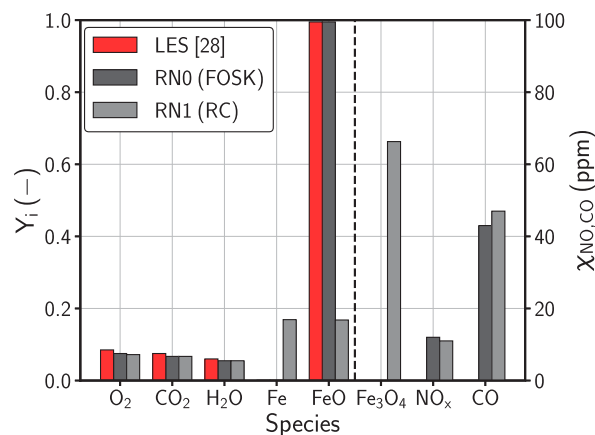

Fig. 10. Major gas species, NOx and CO emissions, and iron(-oxide) mass fractions at the outlet of two CRN simulations conducted with the FOSK model (RN0 (dark gray)) and the RC model (RN1 (gray)), and the reference LES (red). The LES values are averaged in time and space. Mole fractions of NOx and CO as well as the mass fraction of Fe_3O_4 are not available from the LES as indicated by the dotted line.

The flow distribution and global mixing of the combustor are incorporated into the CRN by means of a residence time distribution (RTD) optimization routine. The objective of the routine is to match the RTD of the CRN to the RTD from experiments or CFD. By optimizing the flow splitting ratios of the splitter units, the deviation from the reference curve is minimized [31,32,55]. Since experimental data on the RTD for the iron–methane operating condition is not available, the probability density function (PDF) of the particle residence times from the LES is used as a reference. The PDF at the outlet can be considered a solid phase RTD since the residence times are referenced to the inlet of the combustor. It is assumed, that particles and gas phase have the same RTD within the CRN. The same assumption has been made by various authors in pulverized coal combustion [32,56], and recently, iron powder combustion [29]. Fig. 9 depicts the PDF of particle residence times from CFD and the CRN-RTD obtained with the optimization routine. The upper (SR3−) and the lower lines (SR3+) mark borders for the maximum change in RTD response during splitting ratio variations of $\pm 10\%$. Overall, the RTD of the CRN is in good agreement with the PDF. Despite the different peak positions observed during the splitting ratio modifications, the mean global residence times remain within a comparable range. The impact of splitting ratio variations on the CRN output is further discussed in Section 4.5.

4.3. Iron conversion and thermochemical states

The presented reactor network is simulated employing two different models for iron particle oxidation. An initial reactor network simulation (RN0) has been conducted using the FOSK model for particle conversion, to enable a direct comparison of the combined iron and methane conversion to the LES. The CRN simulation employing the RC model (RN1) serves as the baseline for further analyses in this work to incorporate additional iron combustion physics, specifically oxidation to Fe_3O_4 and evaporation of liquid iron(-oxides).

Fig. 10 depicts the gas phase composition of major species, NOx, CO, and the iron(-oxide) mass fractions at the outlet of the configuration, compared to the LES results. In general, the major gaseous species are in accurate agreement for both CRN simulations. The noticeable difference in the iron mass fractions of the two CRN simulations is related to further oxidation from FeO to Fe_3O_4 considered with the reactive cooling model. Despite the same network configuration, the competition for oxygen between both oxidation reactions results in lower iron conversion. The amount of NOx and CO emissions is similar in both CRN simulations, which is attributed to the same network parameters for the gas phase. Following the global validation of the CRN, the investigations in the next sections are conducted on the basis of RN1, employing the reactive cooling model with an initial particle size of 7.7 μm.

4.4. Sensitivities of particle conversion and evaporation with respect to particle size

In order to understand the impact of the mean particle diameter on the conversion behavior, five distinct particle initial diameters (5, 7.7, 10, 15 and 20 μm) are investigated.

In Fig. 11(a), oxygen and iron(-oxide) mass fractions at the outlets of selected reactors from the CRN calculated with different initial particle diameters are compared to the oxygen distribution from the LES data in Fig. 11(b). For better visualization, the data of the simulations with the smallest and largest initial particle size in addition to the baseline case (RN1) are displayed. Within the iron CRNs, the selected reactors are located along the center line of the combustor. The oxygen entering each reactor undergoes complete conversion. Despite the high temperatures, only approximately 30% of the iron is converted in the quarl region, since the oxygen from the primary and secondary streams in R2 is already consumed by the faster-reacting methane flame. At the outlet of R1, all solid species are molten and converted to liquid iron(oxides) at these elevated temperatures. A comparable scenario can be seen for FeO in the case of R4, R5, and R6. Additional oxygen for further particle conversion below the quarl is supplied by the tertiary stream. At the exit of the CRNs, the solids consist mainly of Fe_3O_4. The iron powder is not fully converted with residual Fe and FeO remaining. Surprisingly, the conversion of iron at different sizes is similar. It can be concluded that the varying heating rate of particles of differing sizes is not the critical parameter for global iron conversion within the CRN. The oxygen is fully consumed by the particles situated at the centerline, due to the rapid kinetics of iron oxidation in comparison to the residence times in the reactors. Therefore, the local oxygen availability as the potential dominant factor for particle conversion inside the combustion chamber is further investigated by adapting the splitting ratios in Section 4.5.

As previously noted, iron particles rapidly reach a liquid state, leading to partial evaporation into the surrounding environment. Given the importance of understanding and controlling this process for iron combustion technology, further analysis of this phenomenon is provided. Fig. 12 shows the accumulated, percentage amount of evaporated mass with respect to the initial solid mass in centerline plugflow reactors for the five CRN simulations with different particle sizes. In all simulations, the evaporation results from the reactors situated at the centerline. The comparable lower gas phase temperature of R9 suppresses evaporation in this region of the CRN. In contrast to iron particle conversion, the amount of evaporation is highly sensitive to the
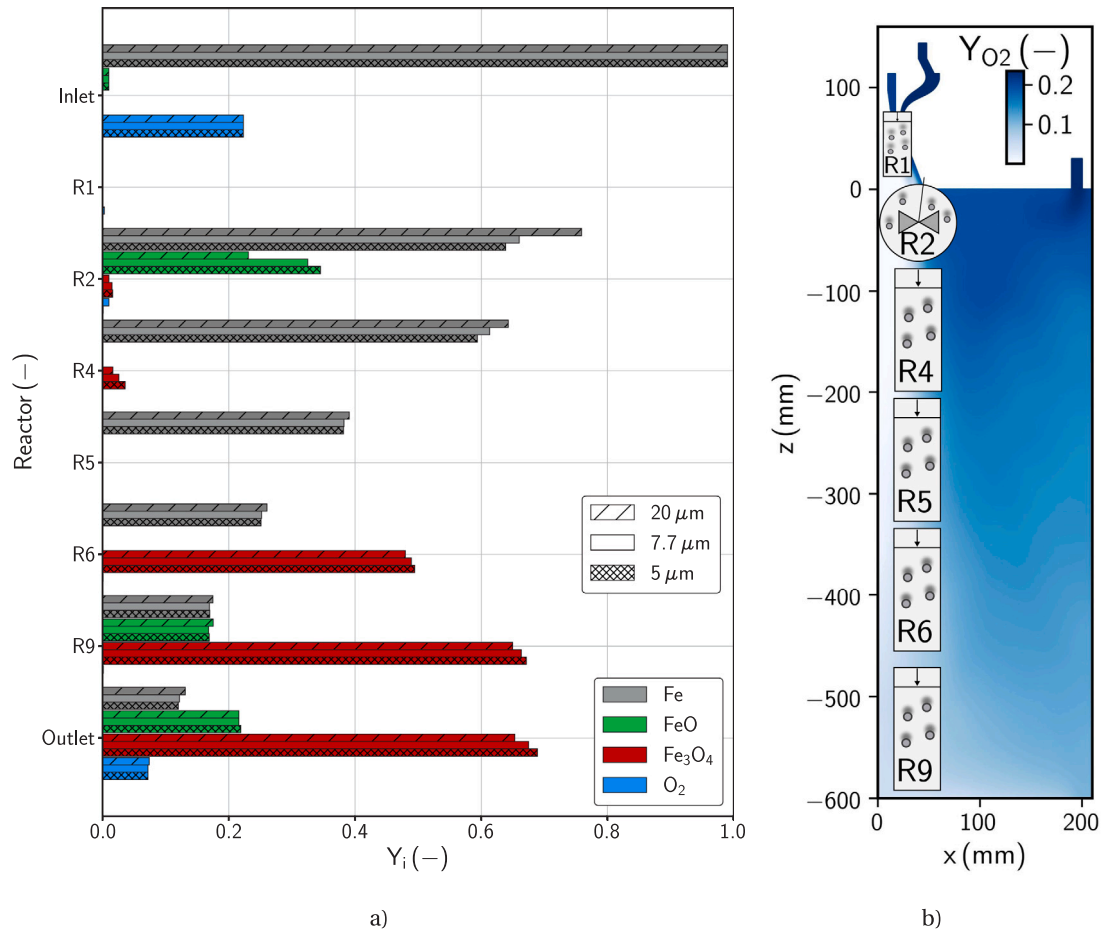
Fig. 11. Species profiles of iron(-oxide) species and oxygen over the height of the combustion chamber: (a) Results from CRN simulations with particle sizes of 5, 7.7 and 20 μm. (b) Centrally positioned reactors on top of the oxygen mass fraction field from LES. Liquid species at elevated temperatures (e.g. FeO in R4, R5 and R6) are not displayed in (a).
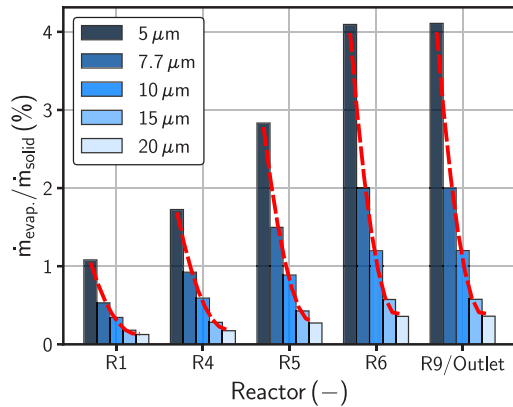

Fig. 12. Accumulated, percentage amount of evaporated mass with respect to the initial solid mass in centerline plug flow reactors with different initial particle sizes. The dashed red lines show a quadratic fit to the bars in each reactor.

initial diameter. Whereas around 0.5% of the initial solids evaporate choosing a diameter of 20 μm, more than 4% evaporate in case of 5 μm particles. In single particle simulations wherein particles are completely converted at comparable oxygen concentrations, Mich et al. [7] report about 8% of evaporated mass. A lower amount is expected in this configuration, given that the particles locally lack the oxygen required for full conversion and thus are unable to attain sufficient temperatures.

The red, dashed lines illustrate a quadratic increase in evaporated mass with decreasing particle size. According to Eq. (11), the single

particle model indicates that evaporation increases linearly with diameter. Conversely, the number of particles is inversely proportional to the cubic diameter, with mass conservation applied to the solid inlet stream. When these dependencies are combined, an overall quadratic dependency for decreasing diameter becomes apparent. In the current CRN modeling approach, the rate of evaporation is determined solely by the diameter of the molten particles when they are subjected to the same residence times. In this case, larger particles result in a reduction in the overall rate of evaporation.

4.5. Flow splitting sensitivity

Previous analyses suggest a strong impact of local oxygen availability on iron particle conversion. Therefore, the sensitivity of the oxygen distribution and mixing inside the CRN on the particle conversion and evaporation is analyzed in this section. The splitting ratios of six selected splitting units in the reactor network are increased and decreased by ± 5 and 10%, respectively. The influence of the variations in splitting ratios on the global flow behavior is implied in Fig. 9 by the gray area. Variations above 10% are not considered, as it was found that the RTD was significantly affected by larger changes.

The approximate locations of the splitters within the CRN are depicted in Fig. 8. The splitters S1 and S4 through S6 account for the mixing of the tertiary oxidizer throughout the combustor below the dump level, affecting the conversion below the diffuser. Splitter S2 distributes the multiphase flow between the centerline and the large outer recirculation zone and S3 determines the amount of recycling in this region.
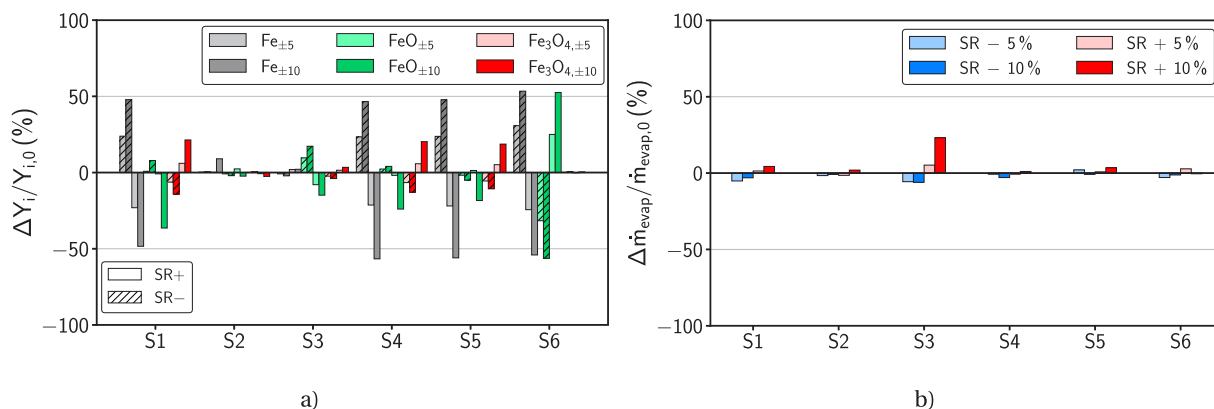
Fig. 13. Sensitivity studies with respect to variations in splitting ratios of ± 5 and 10% at selected splitting units and their impact on iron conversion (a) and evaporation (b) at the outlet of RN1.

Fig. 13(a) depicts the varying mass fractions of the respective iron(-oxides) at the outlet of the combustor when changing a single splitting ratio. The largest sensitivities are visible for S1 and S4 to S6. The amount of excess iron decreases if more oxygen from the tertiary stream is fed to the reactors located downstream. While the mass fraction of FeO drastically changes in the case of S6, the other splitting ratios have a larger impact on Fe_3O_4 formation. This is related to the local oxygen availability within CRN. For S6, a large portion of remaining iron is oxidized to FeO due to lower temperatures and insufficient residence times in comparison to the upper and center parts of the chamber. If more oxygen is exposed to the reactors located in the upper part (R4, R5) or into the recycling region, more iron particles are fully converted to Fe_3O_4. Lower sensitivities are observed for S2 and S3. The amount of recycling (S3) affects the oxidation from FeO to Fe_3O_4. A larger portion of solids is exposed to the elevated temperatures in R6, which leads to further conversion in this case. In general, the mixing of oxygen originating from the tertiary stream is a critical parameter for particle conversion inside the combustion chamber.

Fig. 13(b) displays the sensitivities of local oxygen availability with respect to evaporation. Compared to the iron conversion, lower sensitivities on evaporation within the CRN are observed. The amount of oxygen from the tertiary stream has a relatively minor impact on the peak temperatures, which can be attributed to the rich mixture and heat losses to the surrounding gases. This results in similar ranges of evaporated mass. Conversely, the influence of recycling is becoming more dominant, which is associated with the increased mass of particles subjected to high-temperature regions.

4.6. Gas temperature sensitivities

Besides particulate pollutants resulting from evaporation, NOx (and in gas-assisted combustion CO) are important gaseous pollutants that need to be controlled during iron combustion. The impact of local gas temperatures on evaporation and NOx formation within the reactor network is investigated in the following. Therefore, the gas temperatures of each reactor are in- and decreased by 5 and 10%, respectively. For visualization purposes, only the sensitivities of reactors R1 to R6 are shown. Temperature changes in reactors downstream from R6 show hardly any sensitivity with respect to the selected quantities of interest due to insufficient temperatures for evaporation and thermal NOx.

Fig. 14(a) displays the sensitivity of local gas temperatures to evaporation. The rate of evaporation is highly sensitive to temperature changes in the plug flow reactors located in regions of elevated temperature at the quarl side and along the centerline. In a further increase, gas temperatures beyond 2000 K are present in the reactors, leading to almost doubled evaporation inside the CRN. A decrease yields gas temperatures below 1800 K, which causes the solidification of Fe and Fe_3O_4, thereby reducing the evaporation in the individual reactors. It

can be concluded that control of local temperature peaks is essential to mitigate evaporation and subsequent nanoparticle formation. The s-PSR R2, which accounts for the IRZ, also exhibits elevated temperatures of the gas phase. However, the particles do not reach sufficient temperatures to affect evaporation significantly.

An additional pollutant of concern in iron combustion is NOx, which is analyzed in Fig. 14(b). In iron dust flames, thermal NOx originating from atmospheric nitrogen is the primary source of NOx emissions [1]. Recent studies have investigated NOx formation [29,57,58] in iron–air flames, while in this work, the assisting methane flame additionally affects pollutant formation. The experimentally determined NOx values at the outlet of a laboratory-scale iron–air burner are below 10 ppm [57], exhibiting a comparable order of magnitude to that observed in RN1, as illustrated in Fig. 10. Reactors R1 and R2 show a substantial increase when higher temperatures are assigned, which is consistent with theory. At gas temperatures above 1800 K, the formation of thermal NOx increases drastically [59].

The sensitivity analyses highlight the necessity for an accurate estimation of local, particularly peak gas temperatures to predict evaporation and NOx emissions within the reactor network. In general, the CRN study suggests that for iron combustion, avoiding locally increased temperatures mitigates both NOx emissions and evaporated mass inside the laboratory-scale burner.

5. Conclusions

This study extends the reactor network approach to the actively researched field of iron combustion. The novel methodology and its implementation is validated in simplified test cases and subsequently applied to a novel gas-assisted iron dust flame within a laboratory-scale combustion chamber to analyze evaporation and NOx emissions.

Following the successful verification of single particle combustion, the flame structure of laminar iron flames has been investigated using novel iron reactor models. It was found that the oxygen profile from reference simulations could not be accurately matched with a single s-PFR simulation. Therefore, a reactor network consisting of multiple interconnected s-PSRs has been introduced to account for the structure of laminar iron flames. This configuration matches the profiles of major species from the references and is therefore suitable for modeling the supporting methane flame.

After the design of the CRN including iron reactor models and successful validation against the reference CFD simulation of the gas-assisted iron swirl flame, comprehensive sensitivity studies have been performed. The results of sensitivity studies on the initial particle size, flow splitting and gas temperature lead to the following conclusions:
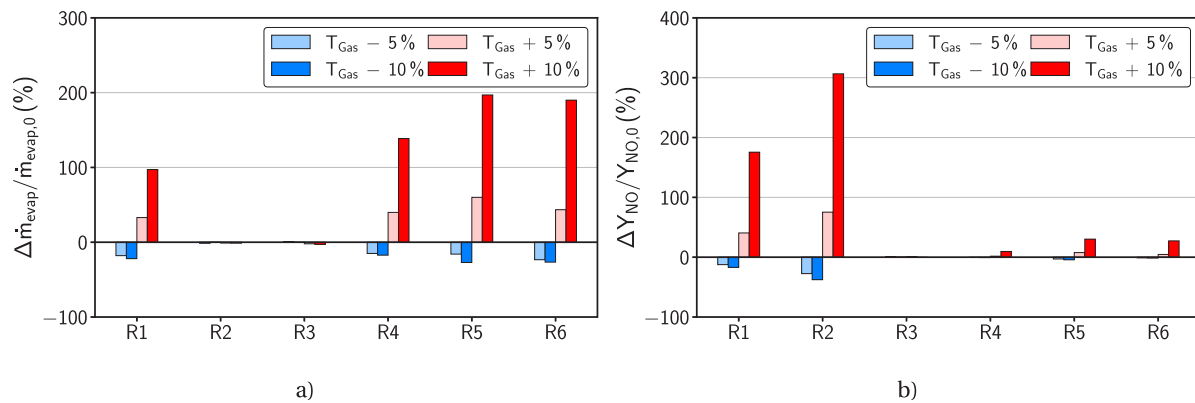
Fig. 14. Sensitivity study with respect to temperature changes of ± 10% from R1 to R6 and their impact on the accumulated evaporation (a) and NOx emissions (b) within RN1.

- While the particle size exhibits a minor impact on the global iron oxidation, major differences in the total evaporation rate are obtained within the CRN simulations. The solid stream consisting of smaller particles leads to increased evaporation.
- The availability of local oxygen has a significant effect on the global conversion of iron particles, but rather little impact on evaporation. The further oxidation of FeO to Fe_3O_4 largely affects the global conversion within the CRN and should be also considered in future CFD simulations.
- Local gas temperatures have a large impact on the evaporation rate and NOx formation within the CRN. Avoiding locally increased temperatures mitigates both NOx emissions and evaporation.

The proposed CRN model is derived from the flow and temperature fields of a specific set of operating conditions. In principle, it can be extended to varying operating conditions under the assumption of similar flow and temperature fields. However, even if the reactor locations within the CRN remain similar, variations in local residence times and, in particular, temperatures can significantly affect the particle conversion and pollutant formation, as demonstrated in the reported sensitivity analyses. The extrapolation to different operating conditions remains an active area of research and has been investigated by other authors [60–62]. The advancements in CRN modeling demonstrated in this study underscore its potential as a powerful tool for predicting gaseous and particulate pollutant formation, paving the way for further exploration and refinement in future research.

CRediT authorship contribution statement

Sören Dübal: Writing – original draft, Visualization, Validation, Software, Methodology, Investigation, Formal analysis, Data curation, Conceptualization. **Pascal Steffens:** Validation, Software, Investigation, Formal analysis, Data curation. **Johannes Mich:** Writing – review & editing, Validation, Software, Data curation. **Daniel Braig:** Validation, Software, Data curation. **Antje Vahl:** Validation, Software, Data curation. **Leon L. Berkel:** Writing – review & editing, Software, Methodology, Investigation. **Arne Scholtissek:** Writing – review & editing, Supervision, Project administration. **Tiziano Faravelli:** Writing – review & editing, Software, Methodology, Investigation. **Christian Hasse:** Supervision, Resources, Project administration, Investigation, Funding acquisition. **Hendrik Nicolai:** Writing – review & editing, Supervision, Software, Project administration, Methodology, Investigation, Formal analysis, Conceptualization. **Sandra Hartl:** Writing – review & editing, Supervision, Resources, Project administration, Investigation, Funding acquisition, Conceptualization.

Declaration of competing interest

The authors declare that they have no known competing financial interests or personal relationships that could have appeared to influence the work reported in this paper.

Data availability

Data will be made available on request.

References

[1] J.M. Bergthorson, S. Goroshin, M.J. Soo, P. Julien, J. Palecka, D.L. Frost, D.J. Jarvis, Direct combustion of recyclable metal fuels for zero-carbon heat and power, Appl. Energy 160 (2015) 368–382.

[2] P. Debiagi, R.C. Rocha, A. Scholtissek, J. Janicka, C. Hasse, Iron as a sustainable chemical carrier of renewable energy: Analysis of opportunities and challenges for retrofitting coal-fired power plants, Renew. Sustain. Energy Rev. 165 (2022) 112579.

[3] J. Janicka, P. Debiagi, A. Scholtissek, A. Dreizler, B. Epple, R. Pawellek, A. Maltsev, C. Hasse, The potential of retrofitting existing coal power plants: A case study for operation with green iron, Appl. Energy 339 (2023) 120950.

[4] J. Neumann, Q. Fradet, A. Scholtissek, F. Dammel, U. Riedel, A. Dreizler, C. Hasse, P. Stephan, Thermodynamic assessment of an iron-based circular energy economy for carbon-free power supply, Appl. Energy 368 (2024) 123476.

[5] P. Julien, J.M. Bergthorson, Enabling the metal fuel economy: Green recycling of metal fuels, Sustain. Energy Fuels 1 (3) (2017) 615–625.

[6] S. Goroshin, J. Palečka, J.M. Bergthorson, Some fundamental aspects of laminar flames in nonvolatile solid fuel suspensions, Prog. Energy Combust. Sci. 91 (2022) 100994.

[7] J. Mich, A.K. da Silva, D. Ning, T. Li, D. Raabe, B. Böhm, A. Dreizler, C. Hasse, A. Scholtissek, Modeling the oxidation of iron microparticles during the reactive cooling phase, Proc. Combust. Inst. 40 (1) (2024) 105538.

[8] F.H. Vance, A. Scholtissek, H. Nicolai, C. Hasse, Flame propagation modes for iron particle clusters in air — Part I: Transition from continuous to discrete propagation mode under weak convection effects, Combust. Flame 260 (2024) 113265.

[9] F.H. Vance, A. Scholtissek, H. Nicolai, C. Hasse, Flame propagation modes for iron particle clusters in air, part II: Transition from continuous to discrete propagation mode under strong convection effects, Combust. Flame 265 (2024) 113199.

[10] G. Thäter, M. Carbone, T.-D. Luu, O.T. Stein, B. Frohnapfel, The influence of clustering in homogeneous isotropic turbulence on the ignition behavior of iron particles, Proc. Combust. Inst. 40 (1) (2024) 105348.

[11] T.D. Luu, A. Shamooni, A. Kronenburg, D. Braig, J. Mich, B.-D. Nguyen, A. Scholtissek, C. Hasse, G. Thäter, M. Carbone, B. Frohnapfel, O.T. Stein, Carrier-phase DNS of ignition and combustion of iron particles in a turbulent mixing layer, Flow Turbul. Combust. 112 (4) (2024) 1083–1103.

[12] T. Luu, A. Shamooni, A. Kronenburg, D. Braig, J. Mich, B.-D. Nguyen, A. Scholtissek, C. Hasse, G. Thäter, M. Carbone, B. Frohnapfel, O. Stein, Carrier-phase DNS study of particle size distribution effects on iron particle ignition in a turbulent mixing layer, Proc. Combust. Inst. 40 (1) (2024) 105297.

[13] J. Mich, D. Braig, T. Gustmann, C. Hasse, A. Scholtissek, A comparison of mechanistic models for the combustion of iron microparticles and their application to polydisperse iron–air suspensions, Combust. Flame 256 (2023) 112949.

[14] T. Hazenberg, J.A. van Oijen, Structures and burning velocities of flames in iron aerosols, Proc. Combust. Inst. 38 (3) (2021) 4383–4390.

[15] X. Mi, A. Fujinawa, J.M. Bergthorson, A quantitative analysis of the ignition characteristics of fine iron particles, Combust. Flame 240 (2022) 112011.

[16] C. van Gool, L. Thijs, W. Ramaekers, J. van Oijen, L. de Goey, Particle equilibrium composition model for iron dust combustion, Appl. Energy Combust. Sci. 13 (2023) 100115.

[17] C. Hasse, P. Debiagi, X. Wen, K. Hildebrandt, M. Vascellari, T. Faravelli, Advanced modeling approaches for CFD simulations of coal combustion and gasification, Prog. Energy Combust. Sci. 86 (2021) 100938.

[18] H. Nicolai, P. Debiagi, X. Wen, L. Dressler, A. Massmeyer, J. Janicka, C. Hasse, Flamelet LES of swirl-stabilized oxy-fuel flames using directly coupled multi-step solid fuel kinetics, Combust. Flame 241 (2022) 112062.

[19] F.H. Vance, A. Scholtissek, H. Nicolai, C. Hasse, A numerical analysis of multi-dimensional iron flame propagation using boundary-layer resolved simulations, Fuel 369 (2024) 131793.

[20] B.-D. Nguyen, D. Braig, A. Scholtissek, D. Ning, T. Li, A. Dreizler, C. Hasse, Ignition and kinetic-limited oxidation analysis of single iron microparticles in hot laminar flows, Fuel 371 (2024) 131866.

[21] C. van Gool, T. Hazenberg, J. van Oijen, L. de Goey, Numerical determination of iron dust laminar flame speeds with the counter-flow twin-flame technique, Combust. Flame 266 (2024) 113524.

[22] D. Ning, Y. Shoshin, J.A. van Oijen, G. Finotello, L. de Goey, Burn time and combustion regime of laser-ignited single iron particle, Combust. Flame 230 (2021) 111424.

[23] D. Ning, Y. Shoshin, M. van Stiphout, J. van Oijen, G. Finotello, P. de Goey, Temperature and phase transitions of laser-ignited single iron particle, Combust. Flame 236 (2022) 111801.

[24] D. Ning, Y. Shoshin, J. van Oijen, G. Finotello, P. de Goey, Size evolution during laser-ignited single iron particle combustion, Proc. Combust. Inst. 39 (3) (2023) 3561–3571.

[25] T. Li, F. Heck, F. Reinauer, B. Böhm, A. Dreizler, Visualizing particle melting and nanoparticle formation during single iron particle oxidation with multi-parameter optical diagnostics, Combust. Flame 245 (2022) 112357.

[26] A. Panahi, D. Chang, M. Schiemann, A. Fujinawa, X. Mi, J.M. Bergthorson, Y.A. Levendis, Combustion behavior of single iron particles-part I: An experimental study in a drop-tube furnace under high heating rates and high temperatures, Appl. Energy Combust. Sci. 13 (2023) 100097.

[27] T. Krenn, T. Li, J. Hebel, B. Böhm, A. Dreizler, Evaluation of a novel measurement method for the laminar burning speed in laminar lifted iron dust flames, Fuel 366 (2024) 131266.

[28] P. Steffens, J. Hebel, D. Braig, A. Vahl, L.L. Berkel, H. Schneider, H. Nicolai, A. Scholtissek, B. Böhm, A. Dreizler, C. Hasse, Experiments and large eddy simulation of a 47 kWth swirl-stabilized methane-assisted iron dust flame (submitted for publication to Fuel).

[29] L.C. Thijs, T. Hazenberg, J.A. van Oijen, P. de Goey, A numerical study of emission control strategies in an iron powder burner, Proc. Combust. Inst. 40 (1) (2024) 105474.

[30] T. Faravelli, L. Bua, A. Frassoldati, A. Antifora, L. Tognotti, E. Ranzi, A new procedure for predicting NOx emissions from furnaces, Comput. Chem. Eng. 25 (4) (2001) 613–618.

[31] S. Trespi, H. Nicolai, P. Debiagi, J. Janicka, A. Dreizler, C. Hasse, T. Faravelli, Development and application of an efficient chemical reactor network model for oxy-fuel combustion, Energy Fuels 35 (9) (2021) 7121–7132.

[32] S. Dübal, L.L. Berkel, P. Debiagi, H. Nicolai, T. Faravelli, C. Hasse, S. Hartl, Chemical reactor network modeling in the context of solid fuel combustion under oxy-fuel atmospheres, Fuel 364 (2024) 131096.

[33] L.L. Berkel, P. Debiagi, H. Nicolai, M.A. Amjed, A. Stagni, C. Hasse, T. Faravelli, Development of a multiphase chemical reactor network method as a tool for simulating biomass gasification in fluidized beds, Fuel 357 (2024) 129731.

[34] P. Debiagi, C. Ontyd, S. Pielsticker, M. Schiemann, T. Faravelli, R. Kneer, C. Hasse, V. Scherer, Calibration and validation of a comprehensive kinetic model of coal conversion in inert, air and oxy-fuel conditions using data from multiple test rigs, Fuel 290 (2021) 119682.

[35] L. Thijs, C. van Gool, W. Ramaekers, J. van Oijen, L. de Goey, Resolved simulations of single iron particle combustion and the release of nano-particles, Proc. Combust. Inst. 39 (3) (2023) 3551–3559.

[36] T. Maffei, R. Khatami, S. Pierucci, T. Faravelli, E. Ranzi, Y.A. Levendis, Experimental and modeling study of single coal particle combustion in O_2/N_2 and oxy-fuel (O_2/CO_2) atmospheres, Combust. Flame 160 (11) (2013) 2559–2572.

[37] P.E.A. Debiagi, C. Pecchi, G. Gentile, A. Frassoldati, A. Cuoci, T. Faravelli, E. Ranzi, Extractives extend the applicability of multistep kinetic scheme of biomass pyrolysis, Energy Fuels 29 (10) (2015) 6544–6555.

[38] M. Soo, S. Goroshin, J.M. Bergthorson, D.L. Frost, Reaction of a particle suspension in a rapidly–heated oxidizing gas, Propellants Explos. Pyrotech 40 (4) (2015) 604–612.

[39] M.J. Soo, K. Kumashiro, S. Goroshin, D.L. Frost, J.M. Bergthorson, Thermal structure and burning velocity of flames in non-volatile fuel suspensions, Proc. Combust. Inst. 36 (2) (2017) 2351–2358.

[40] L.C. Thijs, C.E.A.G. van Gool, W.J.S. Ramaekers, J.G.M. Kuerten, J.A. van Oijen, L.P.H. de Goey, Improvement of heat- and mass transfer modeling for single iron particles combustion using resolved simulations, Combust. Sci. Technol. 196 (4) (2024) 572–588.

[41] W.E. Ranz, W.R. Marshall, Evaporation from drops, Chem. Eng. Prog. (48) (1952) 141–146.

[42] A. Fujinawa, L.C. Thijs, J. Jean-Philyppe, A. Panahi, Di Chang, M. Schiemann, Y.A. Levendis, J.M. Bergthorson, X. Mi, Combustion behavior of single iron particles, part II: A theoretical analysis based on a zero-dimensional model, Appl. Energy Combust. Sci. 14 (2023) 100145.

[43] G. Bagheri, E. Ranzi, M. Pelucchi, A. Parente, A. Frassoldati, T. Faravelli, Comprehensive kinetic study of combustion technologies for low environmental impact: MILD and OXY-fuel combustion of methane, Combust. Flame 212 (2020) 142–155.

[44] I. Wlokas, A. Faccinetto, B. Tribalet, C. Schulz, A. Kempf, Mechanism of iron oxide formation from iron pentacarbonyl-doped low-pressure hydrogen/oxygen flames, Int. J. Chem. Kinet. 45 (8) (2013) 487–498.

[45] M. Nanjaiah, A. Pilipodi-Best, M.R. Lalanne, P. Fjodorow, C. Schulz, S. Cheskis, A. Kempf, I. Wlokas, I. Rahinov, Experimental and numerical investigation of iron-doped flames: FeO formation and impact on flame temperature, Proc. Combust. Inst. 38 (1) (2021) 1249–1257.

[46] A. Cuoci, A. Frassoldati, T. Faravelli, E. Ranzi, OpenSMOKE++: An object-oriented framework for the numerical modeling of reactive systems with detailed kinetic mechanisms, Comput. Phys. Comm. 192 (2015) 237–264.

[47] A. Cuoci, A. Frassoldati, G. Buzzi Ferraris, T. Faravelli, E. Ranzi, The ignition, Combustion and flame structure of carbon monoxide/hydrogen mixtures. note 2: Fluid dynamics and kinetic aspects of syngas combustion, Int. J. Hydrog. Energy 32 (15) (2007) 3486–3500.

[48] D. Manca, G. Buzzi-Ferraris, A. Cuoci, A. Frassoldati, The solution of very large non-linear algebraic systems, Comput. Chem. Eng. 33 (10) (2009) 1727–1734.

[49] A. Stagni, A. Cuoci, A. Frassoldati, T. Faravelli, E. Ranzi, A fully coupled, parallel approach for the post-processing of CFD data through reactor network analysis, Comput. Chem. Eng. 60 (2014) 197–212.

[50] G.P. Smith, D.M. Golden, M. Frenklach, N.W. Moriarty, B. Eiteneer, M. Goldenberg, C.T. Bowman, R.K. Hanson, S.J. Song, W.C. Gardiner, V. Lissianski, Z. Qin, GRI-Mech 3.0: An Optimized Detailed Chemical Kinetics Mechanism for Methane Combustion, GRI, 1999, http://combustion.berkeley.edu/gri-mech/version30/text30.html.

[51] L.G. Becker, H. Kosaka, B. Böhm, S. Doost, R. Knappstein, M. Habermehl, R. Kneer, J. Janicka, A. Dreizler, Experimental investigation of flame stabilization inside the quarl of an oxyfuel swirl burner, Fuel 201 (2017) 124–135.

[52] H. Schneider, S. Valentiner, N. Vorobiev, B. Böhm, M. Schiemann, V. Scherer, R. Kneer, A. Dreizler, Investigation on flow dynamics and temperatures of solid fuel particles in a gas-assisted oxy-fuel combustion chamber, Fuel 286 (2021) 119424.

[53] R. Knappstein, G. Kuenne, L.G. Becker, F. di Mare, A. Sadiki, A. Dreizler, J. Janicka, Large eddy simulation of a novel gas-assisted coal combustion chamber, Flow Turbul. Combust. 101 (3) (2018) 895–926.

[54] H. Nicolai, G. Kuenne, R. Knappstein, H. Schneider, L.G. Becker, C. Hasse, F. Di Mare, A. Dreizler, J. Janicka, Large eddy simulation of a laboratory-scale gas-assisted pulverized coal combustion chamber under oxy-fuel atmospheres using tabulated chemistry, Fuel 272 (2020) 117683.

[55] M.A. Agizza, G. Bagheri, S. Bürkle, T. Faravelli, S. Wagner, A. Dreizler, Investigation of oxy-fuel combustion through reactor network and residence time data, Energies 15 (1) (2022).

[56] S. Bürkle, L.G. Becker, M.A. Agizza, A. Dreizler, S. Wagner, Comparison of two measurement strategies to obtain the residence time distribution in combustion chambers using tunable diode laser absorption spectroscopy, Appl. Opt. 58 (10) (2019).

[57] M. Baigmohammadi, W. Prasidha, N.C. Stevens, Y.L. Shoshyn, T. Spee, P. de Goey, Towards utilization of iron powders for heating and power, Appl. Energy Combust. Sci. 13 (2023) 100116.

[58] A. Ravi, T. Hazenberg, L. Thijs, J. van Oijen, L. de Goey, Nitrogen oxide formation mechanism in iron dust flames, Proc. Combust. Inst. 40 (1) (2024) 105611.

[59] S. Hill, L. Douglas Smoot, Modeling of nitrogen oxides formation and destruction in combustion systems, Prog. Energy Combust. Sci. 26 (4) (2000) 417–458.

[60] M. Savarese, A. Procacci, S. Iavarone, L. Giuntini, W.D. Paepe, A. Parente, A sparse sensing and chemical reactor network based framework for the development of physics-based digital twins of combustion devices, Proc. Combust. Inst. 40 (1) (2024) 105536.

[61] M. Savarese, A. Cuoci, W. De Paepe, A. Parente, Machine learning clustering algorithms for the automatic generation of chemical reactor networks from CFD simulations, Fuel 343 (2023) 127945.

[62] L. Gossel, E. Corbean, S. Dübal, P. Brand, M. Fricke, H. Nicolai, C. Hasse, S. Hartl, S. Ulbrich, D. Bothe, Scale-bridging within a complex model hierarchy for investigation of a metal-fueled circular energy economy by use of Bayesian model calibration with model error quantification, 2024, arXiv:2404.13092.